

# Beam-based optimization of SwissFEL low-level RF system

Zhe-Qiao Geng<sup>1</sup>

Received: 22 March 2018 / Revised: 15 June 2018 / Accepted: 16 June 2018 / Published online: 26 July 2018  
© Shanghai Institute of Applied Physics, Chinese Academy of Sciences, Chinese Nuclear Society, Science Press China and Springer Nature Singapore Pte Ltd. 2018

**Abstract** SwissFEL is a free electron laser (FEL) under commissioning at the Paul Scherrer Institut (PSI) in Switzerland. Digital low-level RF (LLRF) systems are used in SwissFEL to control more than 30 RF stations with either standing wave cavities (e.g. RF gun) or travelling wave structures working at different frequencies. After conditioned to desired power levels, the RF stations need to be setup for beam operation and the LLRF parameters need to be optimized for maximizing the beam stability. Several beam-based algorithms were developed to facilitate the setup, calibration and optimization of the SwissFEL RF stations for beam operation. The algorithms were implemented as automation procedures in the framework of Experimental Physics and Industrial Control System (EPICS) and were used in commissioning and daily operation of SwissFEL. In this paper, the algorithms and the implementation will be introduced together with the test results during the commissioning of SwissFEL.

**Keywords** SwissFEL · LLRF optimization · Beam-based calibration

## 1 Introduction

SwissFEL is a FEL machine based on normal-conducting linear accelerator, and its layout is shown in Fig. 1 [1]. The SwissFEL accelerator employs an S-band RF gun [2] with a 2.6-cell standing wave cavity to generate electron

bunches with a bunch charge up to 200 pC and a beam energy 7.1 MeV. The Booster1 consists of two 4-metre-long S-band travelling wave structures [3] each powered by a separate RF station. A laser heater [4] chicane is used to mitigate micro-bunching instabilities in the bunch compressors. The Booster2 consists of two S-band and one X-band RF stations, each driving two travelling wave structures, respectively. The Booster2 S-band RF stations operate off-crest to generate the required energy chirp for bunch compression in the first bunch compressor, BC1. The X-band RF station works at a decelerating phase to linearize the energy distribution along the electron bunch for optimal compression performance [5]. After BC1, the Linac1 with nine C-band RF stations [6, 7] is used to ramp the beam energy and generate the necessary energy chirp for the second bunch compressor, BC2. Each C-band RF station drives four travelling wave structures. The Linac2 consists of four C-band RF stations which boost the beam energy to 3 GeV to feed the soft X-ray line “Athos” and the Linac3 of the hard X-ray line “Aramis”. In the Aramis beam line, 13 C-band RF stations are used to ramp the electron beam energy up to 5.8 GeV before injection in the undulators.

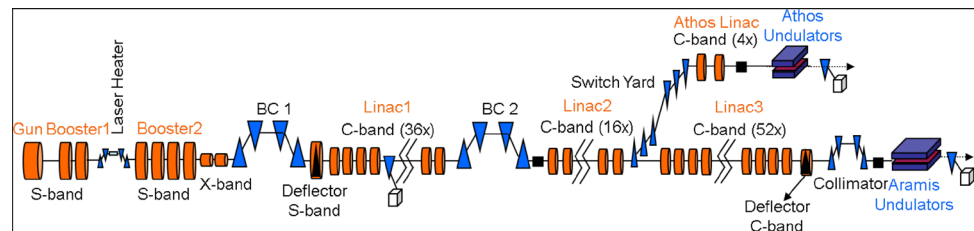
SwissFEL works at a repetition rate of 100 Hz with up to two electron bunches separated by 28 ns in the same RF pulse. The first bunch will feed the Aramis beam line and the second bunch will be picked up to feed the Athos beam line with a fast kicker magnet after Linac2 [8].

SwissFEL requires highly stable electron beams for FEL generation [9]. At the exit of Linac3, the beam energy jitter should be smaller than 0.05% RMS; the peak current fluctuation should be smaller than 5% RMS, and the beam arrival time jitter should be smaller than 5 fs RMS. To minimize the FEL fluctuation, the RF system must satisfy

✉ Zhe-Qiao Geng  
zheqiao.geng@psi.ch

<sup>1</sup> Paul Scherrer Institut (PSI), 5232 Villigen, Switzerland

**Fig. 1** (Color figure online) Layout of SwissFEL linear accelerator



tight requirements on amplitude and phase stabilities as shown in Table 1.

The pulse-to-pulse jitters of the SwissFEL RF system are dominated by the stabilities of klystron driver amplifiers and high-voltage klystron modulators [10]. The RF pulse width (from 100 ns to 3  $\mu$ s) is too short to implement efficient and reliable intra-pulse feedbacks. Pulse-to-pulse feedbacks were implemented in the LLRF system [11] to compensate the RF fluctuations at frequencies from 0.01 to 10 Hz. For longer time intervals, the drifts of the LLRF detection chain must be corrected by the beam-based feedbacks [12].

Each RF station of the SwissFEL RF system is controlled by an independent LLRF node [13]. After completing the RF conditioning, a calibration and optimization procedure applies to each RF station to determine the correct setup for beam operation. The basic steps of the procedure are described below:

1. Setup the beam energy spectrometer. A spectrometer with a bending magnet detects the beam energy changes as a result of the RF–beam interaction.
2. Adjust the timing of the RF station for optimal overlap with the electron beam.
3. Calibrate the beam phase offset. The measurement of RF phase for on-crest acceleration should be detected, and the offset calibration for beam phase can be determined.
4. Adjust the RF measurement average window by identifying the beam interaction region in the RF pulse. This step helps to determine the actual RF field felt by the beam.
5. Optimize the RF feedback loops. The gains of the pulse-to-pulse feedback loops will be optimized to minimize the jitters of beam parameters which are sensitive to the selected RF stations.

The algorithms developed to automate the steps above will be described in detail in the next section together with the test results during the commissioning of SwissFEL.

## 2 RF optimization algorithms

### 2.1 Adjust RF timing

When an RF station is under conditioning, it is operated on a different time slot from the arrival time of electron bunches so that the RF conditioning will not disturb the beam operation. When applying the RF station on beam operation, the timing of the RF station should be adjusted to have a good overlap between the RF pulse and the beam arrival time.

SwissFEL employs an event-based timing system [14]. The event number of the RF station should be firstly assigned to be the one used for beam operation, and then the delay setting in the event receiver (EVR) should be adjusted to roughly align the RF pulse with the beam. Due to the uncertain time of the RF pulse, it usually takes quite long time to overlap the RF and beam for the first time by manually adjusting the EVR delay. To facilitate the RF timing setting, an algorithm was developed to determine the EVR delay automatically as in Fig. 2.

In Fig. 2, it is assumed that a reference RF station has been properly applied on beam operation, and the total delay of the reference RF station counting from the fiducial time of the Event Generator (EVG) can be calculated as:

$$\hat{T}_d = \hat{T}_p + \hat{T}_{\text{EVR}} + \hat{T}_{\text{fine}}, \quad (1)$$

where  $\hat{T}_p$ ,  $\hat{T}_{\text{EVR}}$  and  $\hat{T}_{\text{fine}}$  are the delays of the reference RF station caused by the timing signal path, the EVR delay (with a resolution of about 0.5  $\mu$ s) and the LLRF firmware fine delay (with a resolution of about 4 ns). In order to

**Table 1** Requirements to RF stabilities

RF station type	Frequency (MHz)	Phase stability RMS ( $^\circ$ )	Amplitude stability RMS (%)
S-band	2998.8	0.018	0.018
C-band	5712.0	0.036	0.018
X-band	11,995.2	0.072	0.018

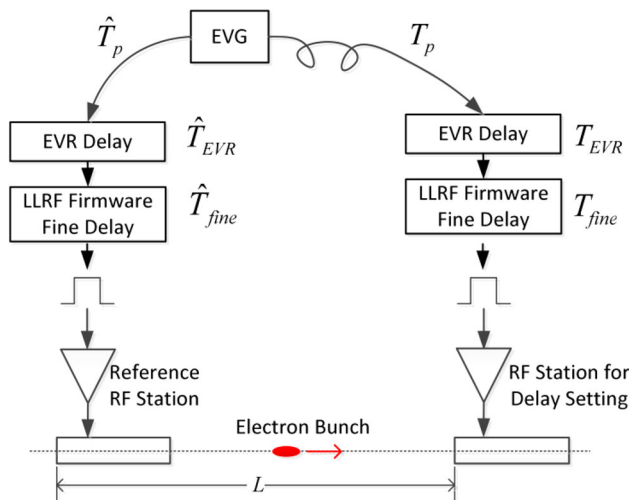


**Fig. 2** (Color figure online) Algorithm to determine EVR delay to align RF and beam

apply the new RF station on beam acceleration, the required total delay can be estimated as

$$T_d = T_p + T_{EVR} + T_{fine} = \hat{T}_d + L/v, \tag{2}$$

where  $L$  is the distance between the RF station and the reference RF station and  $v$  is the speed of the electron bunch which equals approximately to the speed of light in vacuum. The term  $L/v$  corresponds to the beam flight time between the two RF stations. In Eq. (2), the timing signal path delay  $T_p$  is known from the timing system design and then the delay settings for the EVR and LLRF firmware can be determined.

The measurements show that the method above works well to guarantee the rough overlap between the RF and beam. In order to fine optimize the RF delay, the LLRF firmware fine delay can be scanned and correlated with the beam energy. Normally the delay is optimized by maximizing the beam energy. Figure 3 shows the delay-energy correlation of a C-band RF station at Linac1.

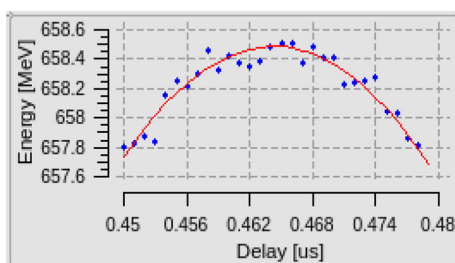


**Fig. 3** (Color figure online) Optimization of RF delay for maximum beam energy. The curve was fitted as a second-order polynomial to find the delay for maximum beam energy

## 2.2 Calibrate beam phase offset

The phase measurements of the RF signals picked up from the accelerating structures have arbitrary values due to the unknown signal paths. The phase offset needs to be calibrated to get the beam phase from the view point of beam dynamics (e.g. beam phase is defined to be  $0^\circ$  with on-crest acceleration).

The calibration is done by scanning the RF phase for maximum beam energy [15, 16]. When the RF station is applied on beam operation for the first time, the beam phase is unknown and the downstream beam optics might not be able to accept large energy variations. To avoid beam losses, the amplitude of the RF station can be set to a smaller value (e.g. 10% of the desired accelerating voltage) within the dynamic range of the downstream beam optics, and the RF phase can be scanned for a full cycle. Figure 4 shows the full-cycle phase scanning of the second RF station in Linac1 correlated with the beam energy.

The relation between the beam energy variation and the phase measurement can be described as

$$\Delta E = V_{acc} \cos(\phi_{mea} + \phi_{off}), \tag{3}$$

where  $V_{acc}$  is the accelerating voltage,  $\phi_{mea}$  is the phase measurement and  $\phi_{off}$  is the phase offset calibration. The beam phase is the sum of  $\phi_{mea}$  and  $\phi_{off}$ . For the  $n$ th measurement point in the phase scanning, Eq. (3) can be rewritten as

$$\Delta E(n) = a \cos(\phi_{mea}(n)) + b \sin(\phi_{mea}(n)), \tag{4}$$

where

$$a = V_{acc} \cos \phi_{off}, \quad b = -V_{acc} \sin \phi_{off}. \tag{5}$$

The parameters  $a$  and  $b$  can be calculated by multi-variable linear fitting according to Eq. (4), and then we get

$$V_{acc} = \sqrt{a^2 + b^2}, \quad \phi_{off} = -\arctan(b/a). \tag{6}$$

Equation (6) shows that the accelerating voltage of the RF station can also be calibrated if the beam energy measurement is accurate. The phase offset calibration is

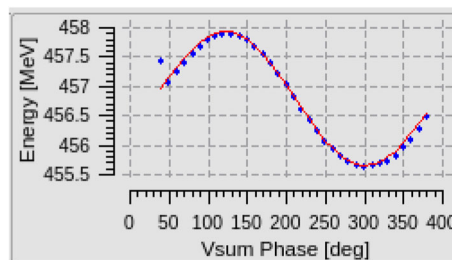


**Fig. 4** (Color figure online) Beam phase offset calibration. The “Vsum Phase” is the vector sum phase measured from the RF signals picked up from the travelling wave structures. The cosine function fitting is also shown in the figure

always valid regardless the accuracy of beam energy measurement.

The beam phase describes the relative timing between the RF and beam arrival time. If the beam arrival time is changed, the phase offset calibration should be updated correspondingly. For a deterministic change of beam flight time from the RF gun to the specific RF station, like due to the adjustment of a chicane, the phase offset calibration can be updated by adding a correction to compensate the change of beam flight time. This situation is depicted in Fig. 5.

The phase offset calibration is performed when the electron bunch passes through the chicane in a straight line (A to D), for which the phase offset is labeled as  $\varphi_{\text{off0}}$ . After the chicane is switched on, the beam passes along the path A, B, C to D, resulting in an increase of the beam flight time ( $\Delta t_f$ ). To keep the beam phase reading still valid, the phase offset calibration should be updated taking into account the delay of beam arrival time:

$$\varphi_{\text{off}} = \varphi_{\text{off0}} + 2\pi f_0 \Delta t_f, \tag{7}$$

where  $f_0$  is the working frequency of the RF station. As an example, the beam flight time through the laser heater of SwissFEL is 3.77 ps, which requires a correction of  $4.07^\circ$  for the phase offset calibrations of the S-band RF stations in Booster2.

### 2.3 Identify RF–beam interaction time

The measurements of RF amplitude and phase should match the RF fields that the beam feels when passing through the accelerating structures. With such accurate RF measurements, the beam can be stabilized by stabilizing the RF and the beam jitters can be estimated by measuring the RF jitters. For a travelling wave structure, the RF pulse width is usually larger than the filling time of the structure. The most important step to achieve the accurate RF measurements is to determine which part of the RF pulse is used for beam acceleration.

Figure 6 shows the filling procedure of a travelling wave structure. The RF power at the early part of the pulse ( $T_1$ ) enters the structure and travels to the loaded end with a

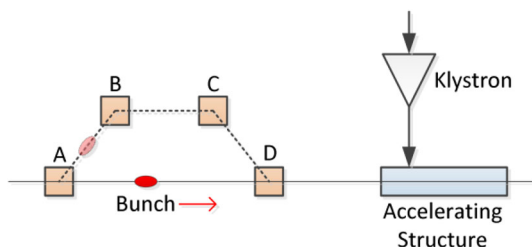


**Fig. 5** (Color figure online) Change of beam flight time when passing through a chicane. A, B, C and D are dipole magnets

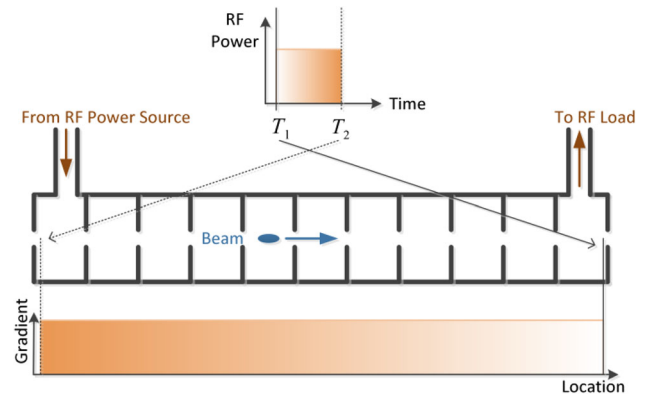


**Fig. 6** (Color figure online) Filling procedure of a travelling wave structure

decaying group velocity along the constant gradient travelling wave structure [3]. When the RF power injected at  $T_1$  arrives at the load and the power at  $T_2$  just enters the structure, the beam is injected. And because the beam travels at a speed (close to the speed of light in vacuum) much higher than the RF group velocity, the beam flight time through the structure can be neglected. Then the RF pulse region from  $T_1$  to  $T_2$  is the RF–beam interaction region used for beam acceleration and  $T_2 - T_1$  equals to the structure filling time. The RF field felt by the beam can be calculated as

$$\mathbf{V}_{\text{acc}} = \int_{T_1}^{T_2} \mathbf{V}_{\text{RF}}(t) dt, \tag{8}$$

where  $\mathbf{V}_{\text{RF}}(t)$  is the measurement of the RF pulse as a time varying vector which can be represented as in-phase ( $I$ ) and quadrature ( $Q$ ) components:  $\mathbf{V}_{\text{RF}}(t) = I(t) + jQ(t)$ . Equation (8) has assumed that different parts of the RF pulse have equal interaction with the beam, which is not true due to the variations of the group velocity (the RF power at time  $T_2$  interacts stronger with the beam than the RF power at  $T_1$ ), but it is still a good approximation of the RF field felt by the beam when we care more the fluctuations of  $\mathbf{V}_{\text{acc}}$ .

In order to identify the RF–beam interaction region in the RF pulse (it is usually wider than the filling time of the structure), a single point in the LLRF DAC output table (DAC works at 250 MSPS) can be reduced to generate a negative bump in the RF power fed into the accelerating structures, see Fig. 7. The time of the RF power bump can be scanned by changing the time of the DAC bump. When the RF power bump appears in the time region between  $T_1$  and  $T_2$ , the beam energy will be reduced. By comparing the beam energy profile when scanning the time of the RF power bump, the RF–beam interaction region in the measurements of the RF pickup

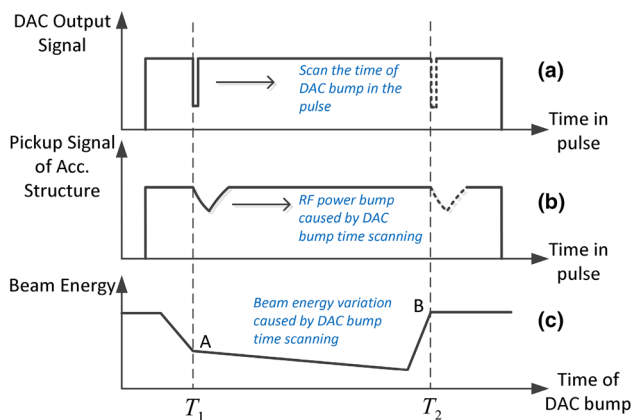


**Fig. 7** (Color figure online) Method to identify RF–beam interaction region in the RF pulse. **a** Time scan of a single-point variation (bump) on DAC output signal; **b** RF power bump generated by the DAC bump appeared in the pickup signals of accelerating structures (both the drive RF and the pickup from RF load); **c** beam energy variations when scanning the time of DAC bump

signals can be identified. The pulse width of the RF power bump will be larger than the DAC clock cycle due to the band-pass filtering by the RF components in the RF system [11]. When the RF power bump is much earlier than  $T_1$ , the beam energy will not be affected; when it approaches to  $T_1$ , the tail of the bump will start to affect the beam energy and after it fully enters the RF–beam interaction region, the beam energy will be affected by the entire bump (see the point A in Fig. 7c). Within the region between  $T_1$  and  $T_2$ , the power bump will reduce more beam energy when it approaches to  $T_2$  because the bump will appear in the location of the accelerating structure with higher group velocity. After the power bump fully exits the RF–beam interaction region (see the point B in Fig. 7c), the beam energy will return to the original value. From the analysis above, the RF–beam interaction region can be identified by finding the points A and B in the beam energy profile.

The algorithm was applied to the last S-band RF station in Booster2. The beam energy was measured by the spectrometer after the first bunch compressor. Figure 8 shows the results of beam energy for different time of the RF power bump. Compared to Fig. 7c, the RF–beam interaction region can be estimated as  $T_1 = 1.30 \mu\text{s}$  and  $T_2 = 2.05 \mu\text{s}$ .

With Eq. (8) the amplitude and phase of the RF signal can be calculated by integrating the RF pulse within the RF–beam interaction region. The vector sum of the  $\mathbf{V}_{\text{acc}}$  measured from the input (picked from the waveguide before the input coupler) and the output (picked from the RF load) of the accelerating structure were used to represent the RF field felt by the beam. To verify the RF–beam interaction region, the beam energy stabilities were measured with the amplitude and phase feedbacks of the last S-

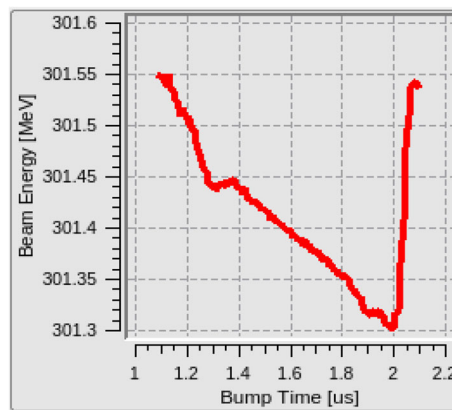


**Fig. 8** (Color figure online) Identification of RF–beam interaction region

band RF station in Booster2 switched on. The effects of feedbacks were compared with different integration windows in the RF pulse, see Fig. 9. In the figure above, the beam energy is represented by the x-position of the electron bunch measured with the BPM after the injector spectrometer. The variation of the beam energy is calculated with the equation

$$\frac{\Delta E}{E_0} = \frac{x}{\eta}, \tag{9}$$

where  $E_0$  is the beam energy when the bunch passes through the BPM center ( $x = 0$ ),  $\Delta E$  is the energy variation,  $x$  is the beam position as shown in Fig. 9 and  $\eta$  is the dispersion length of the spectrometer at the BPM location,

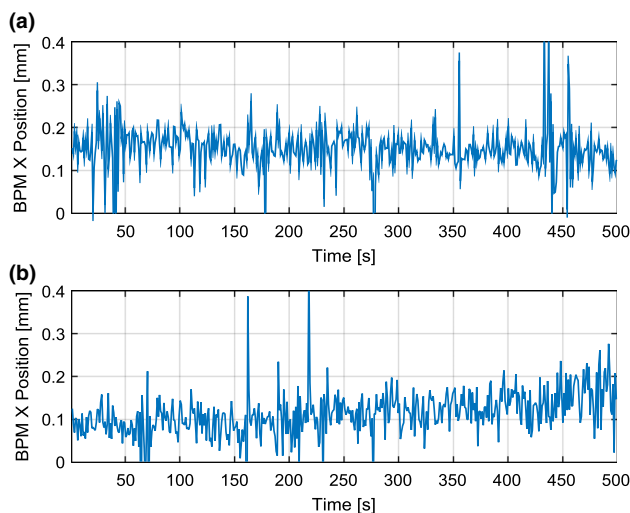


**Fig. 9** (Color figure online) Beam energy stabilities with different integration windows for the RF measurement. The amplitude and phase feedbacks were switched on. When the integration window equaled to the RF–beam integration region as in plot (a), the beam energy stability was  $\Delta E/E_0 = 5.95e-5$  RMS; while when shifting the integration window by 150 ns as in plot (b), the achieved energy stability was  $\Delta E/E_0 = 6.57e-5$  RMS

which has a value of  $\eta = -0.85$  m for the injector spectrometer.

The results in Fig. 9 show that the RF-based feedbacks can help more if the measurement of RF fields matches what the beam feels. As a follow-up plan, the algorithm using Eq. (8) will be improved to take into account the variations of group velocity along the structure.

### 2.4 Optimize RF feedbacks

The SwissFEL LLRF system employs pulse-to-pulse integral feedbacks to stabilize the RF amplitude and phase [10]. The RF station can be viewed as a static system for pulse-to-pulse control because the adjustments of amplitude and phase after one pulse will be fully applied to the next pulse. The block diagram of the feedback loop is shown in Fig. 10 with the system gain normalized to  $G = 1$ .

The pulse-to-pulse amplitude and phase feedbacks have been successfully adopted in SwissFEL to achieve accurate RF settings and maintain long-term RF stabilities. Figure 11 shows the suppression of the amplitude and phase fluctuations in the RF gun field with feedbacks. The Gun phase is more sensitive to the cooling water temperature changes than the amplitude.

The parameters of the feedback loops (e.g. the feedback gains) should be optimized aiming to provide maximum RF stabilities. In order to do the optimization, a brief analysis of the noise transfer model of the feedback loop in Fig. 10 will be firstly performed.

The closed-loop bandwidth of the integral feedback loop will be determined by the gain ( $k$ ) of the discrete integrator  $C$ . The selection of the feedback gain will be a trade-off between the characteristics of the disturbance and measurement noise, the required response speed to reference changes and the feedback stability criteria [17]. The transfers from the disturbance and measurement noise to the system output in frequency domain are shown in Fig. 12a with the gain assigned to  $k = 0.5$ . With higher

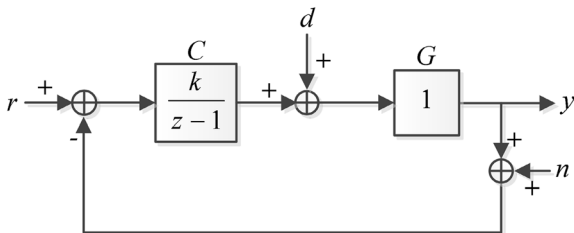


**Fig. 10** Block diagram of the pulse-to-pulse feedback loop.  $r$  is the amplitude or phase reference value,  $d$  is the disturbance to the RF station,  $y$  is the amplitude or phase of the RF output and  $n$  is the measurement noise. The amplitude and phase are measured for each RF pulse with Eq. (8). The sampling time of the discrete transfer functions is the period of RF repetition

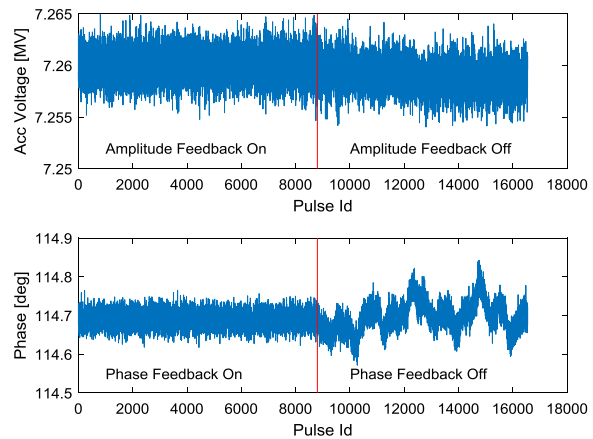


**Fig. 11** (Color figure online) Suppression of RF gun amplitude and phase fluctuations with pulse-to-pulse feedbacks. The Gun works at a repetition rate of 10 Hz

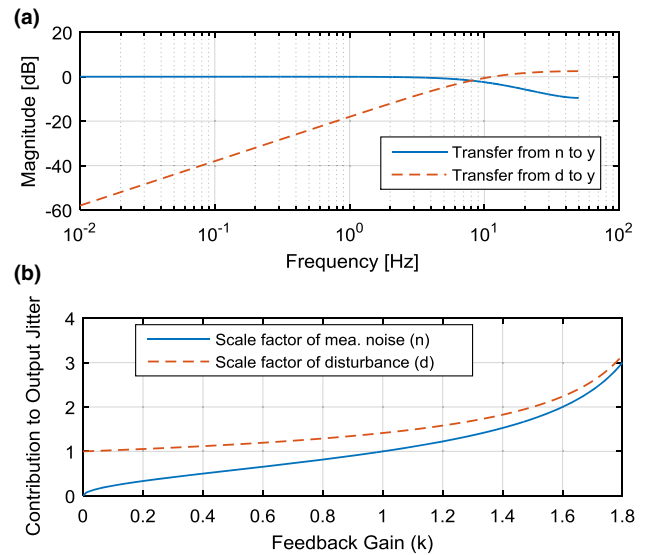


**Fig. 12** (Color figure online) Contributions of disturbance and measurement noise to output jitters. **a** Frequency responses of closed-loop transfer functions from  $n$  to  $y$  and from  $d$  to  $y$  with a feedback gain  $k = 0.5$ ; **b** Contributions of disturbance and measurement noise (both are white noises with RMS values normalized to 1) to system output RMS jitters with different feedback gains. The feedback gain should be smaller than 2 to keep the loop stable

gains, the closed-loop bandwidth, which is the frequency at which the magnitude of the sensitivity function (transfer from  $d$  to  $y$ ) is  $-3$  dB, will be higher. The higher gain will result in more suppression of low-frequency disturbances, faster response to reference changes, but more amplification of high-frequency disturbances and more transfer of measurement noises. For a special case, when the disturbance and measurement noise are both white noises, which have constant power intensities within the Nyquist bandwidth of the RF repetition rate, the RMS jitters in the

system output  $y$  generated by the disturbance  $d$  and measurement noise  $n$  for different feedback gains are plotted in Fig. 12b. Here the RMS values of  $d$  and  $n$  are normalized to 1. It can be seen that if there are no special low-frequency disturbances, the feedbacks will always increase the pulse-to-pulse jitters at the RF output. For a specific low-frequency disturbance (e.g. temperature fluctuation of the cooling water), the closed-loop bandwidth should be larger than the frequency of the disturbance. In practice, the feedback gain can be scanned and the optimal value can be selected for minimum RF or beam jitters as a trade-off between the disturbance rejection and jitter amplification as in Fig. 12b.

The feedback gain optimization algorithm was tested at the X-band RF station of SwissFEL. The RF feedback gains were correlated with both the RF jitters and the bunch length jitters measured after BCI which have strong correlations with the X-band RF [5]. The test results are shown in Fig. 13. The RMS jitters of the amplitude, phase and bunch length were calculated from 100 pulses with an RF repetition rate of 10 Hz, which covers the noise power from 0.05 to 5 Hz (Nyquist bandwidth of the RF repetition rate).

Figure 13 shows that the feedbacks will amplify the RF jitters when the gains are larger than about 0.4. With the spectrums of the X-band amplitude and phase jitters in open loop (see Fig. 14), it can be seen that the noises

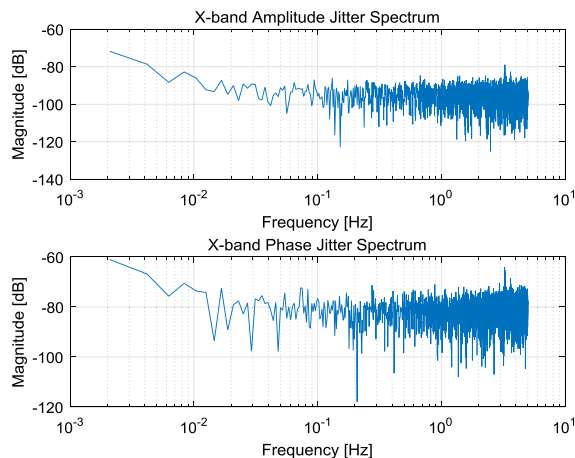


**Fig. 14** (Color figure online) Spectrums of the open-loop amplitude and phase jitters of the X-band RF station

higher than 0.05 Hz are close to white noise, resulting in amplification of the RF jitters with a large feedback gain. Based on the tests and analysis above, the pulse-to-pulse feedback gains of the X-band RF station should be set with the following guidelines:

1. Both the amplitude and phase feedback gains should be small (e.g. 0.1) to only suppress the low-frequency drifts (slower than 0.01 Hz in Fig. 14).
2. When scanning the RF amplitude and phase set points, the feedback gains can be temporarily increased to have faster responses. Feedforward is an alternative to accelerate the response to set point changes.
3. When the RF station is used as an actuator for beam-based feedback, the LLRF system can work in open-loop if the beam-based feedback can cover the same bandwidth as the RF-based feedbacks. This helps to avoid the instabilities caused by the cascaded feedback loops if they have similar closed-loop bandwidths.

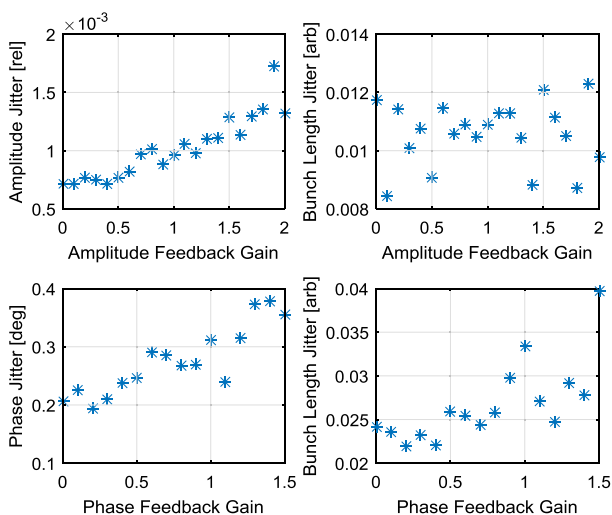


**Fig. 13** (Color figure online) Feedback gain optimization of the X-band RF station referring to both the RF jitters and bunch length jitters. The bunch length jitter is more sensitive to the X-band phase jitter than to the amplitude jitter. This is why the bunch length jitter shows less correlation with the amplitude feedback gains (right-top plot). The larger X-band phase jitter with higher phase feedback gains results in larger bunch length jitter (right-bottom plot), but the correlation is not so strong. This is because the bunch length jitter also depends on the phase jitters of the S-band RF stations upstream to the X-band RF station

### 3 RF optimization software

The LLRF optimization algorithms described in the last section were implemented in a software package as automation procedures. The software was implemented as a soft EPICS input and output controller (IOC) based on the Python language. The software architecture is depicted in Fig. 15.

In the soft IOC, each RF station is optimized by a separate module. The module consists of an execution coordinator, which is driven by a thread, to coordinate the executions of the optimization procedures. A procedure is usually triggered by a command generate by the process of an EPICS record (e.g. click a button on the graphical user

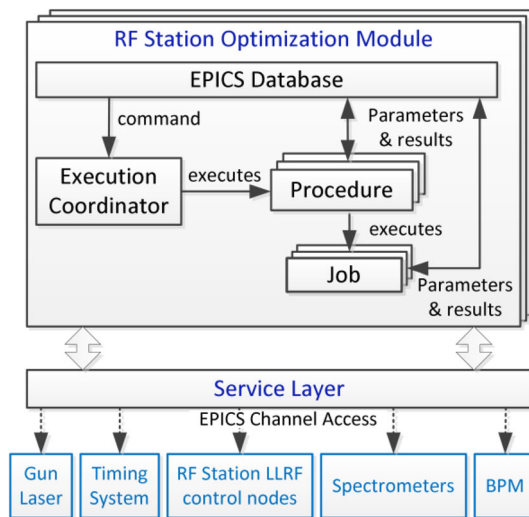


**Fig. 15** (Color figure online) Architecture of the LLRF optimization software

interface). Each procedure contains several steps and each step is designed as a job, for example, each algorithm described in the last section was implemented as a job in a certain procedure. The EPICS database (a collection of records that are accessible via Ethernet) was defined for each module to accept the user inputs and display the results of job executions. All the modules share the same service layer which implemented necessary functions to read the data and write the parameters and commands for the devices in the accelerator, such as the Gun laser, spectrometers and BPMs.

#### 4 Conclusion and outlook

The beam-based optimization algorithms and software tool have been used for the commissioning and daily operation of the LLRF system for SwissFEL. They provided good supports to the LLRF experts to setup new RF stations on beam operation and optimize the LLRF performances. Further optimizations of the LLRF system are in plan to improve the RF measurement accuracy (e.g. by introducing a weight function to Eq. (9) to take into account the group velocity variations in the travelling wave structures), upgrade the pulse-to-pulse control algorithm (e.g. with more complicated feedback algorithm and apply adaptive feed forward controls) and compensate the drifts in RF measurement paths. Python has been proved to be a very efficient language to program the non-real-time automation software with fully supports of EPICS, multi-thread programming and rich mathematic libraries. The software architecture in Fig. 15 and the Python

programming strategy will be applied to other automation software for the future machine controls.

**Acknowledgements** The author would like to thank the SwissFEL LLRF and RF team at the Paul Scherrer Institut to provide high-performance and reliable RF control hardware, firmware and software as a basis for the optimization procedures introduced in this paper.

#### References

1. C.J. Milne, T. Schietinger, M. Aiba et al., SwissFEL: the Swiss X-ray free electron laser. *Appl. Sci.* **7**, 720–776 (2017). <https://doi.org/10.3390/app7070720>
2. U. Ellenberger, H. Blumer, The SwissFEL RF gun: manufacturing and proof of precision by field profile measurements, in *Proceedings of LINAC2014*, Geneva, Switzerland (2014), pp. 1117–1119
3. J. Y. Raguin, The SwissFEL S-band Accelerating Structure: RF Design, in *Proceedings of LINAC2012*, Tel-Aviv, Israel (2012), pp. 498–500
4. M. Pedrozzi, M. Calvi, R. Ischebeck et al., The Laser Heater System of SwissFEL, in *Proceedings of FEL2014*, Basel, Switzerland (2014), pp. 871–877
5. Paul Emma, X-Band RF Harmonic Compensation for Linear Bunch Compression in the LCLS, SLAC-TN-05-004 (2001)
6. F. Loehl, J. Alex, H. Blumer et al., Status of the SwissFEL C-band linear accelerator, in *Proceedings of FEL2013*, New York, USA (2013), pp. 317–321
7. A. Hauff, SwissFEL C-band LLRF prototype system, in *Proceedings of LINAC2014*, Geneva, Switzerland (2014), pp. 683–685
8. R. Ganter, S. Bettoni, H.H. Braun et al. Overview of the soft X-ray line Athos at SwissFEL, in *Proceedings of FEL2017*, Santa Fe, NM, USA (2017)
9. B. Beutner, S. Reiche, Sensitivity and tolerance study for the SwissFEL, in *Proceedings of FEL2010*, Malmo, Sweden (2010), pp. 437–440
10. Z. Geng, B. Hong, Design and calibration of an RF actuator for low-level RF systems. *IEEE Trans. Nucl. Sci.* **63**, 281–287 (2016). <https://doi.org/10.1109/TNS.2015.2507204>
11. Z. Geng, RF control optimization and automation for normal conducting linear accelerators. *IEEE Trans. Nucl. Sci.* **64**, 2361–2368 (2016). <https://doi.org/10.1109/TNS.2017.2723508>
12. D. Fairley, K. Kim, K. Luchini et al., Beam based feedback for the linac coherent light source, in *Proceedings of ICALEPCS2011*, Grenoble, France (2011), pp. 1310–1313
13. Z. Geng, Architecture design for the SwissFEL LLRF system, in *Proceedings of LINAC2014*, Geneva, Switzerland (2014), pp. 1114–1116
14. B. Kalantari, R. Biffiger, SwissFEL timing system: first operational experience, in *Proceedings of ICALEPCS2017*, Barcelona, Spain (2017)
15. R.K. Jobe, N. Phinney et al., Phasing tools for the Klystron at the SLC, in *Proceedings of PAC1989*, Chicago, IL, USA (1989), pp. 1984–1986
16. J.R. Bogart, R.W. Assmann, M. Breidenbach et al., A fast and accurate phasing algorithm for the RF accelerating voltages of the SLAC linac, in *Proceedings of EPAC98*, Stockholm, Sweden (1998), pp. 448–450
17. R.C. Dorf, R.H. Bishop, *Modern Control Systems* (Pearson Education Inc, London, 2016)